2013-12-09

Polarization Diversity in the Presence of Multipath Propagation

Grant Taylor Wagner
Brigham Young University - Provo

Polarization Diversity in the Presence of Multipath Propagation

Grant T. Wagner

A thesis submitted to the faculty of
Brigham Young University
in partial fulfillment of the requirements for the degree of

Master of Science

Michael D. Rice, Chair
Neal K. Bangerter
Brian D. Jeffs

Department of Electrical and Computer Engineering

Brigham Young University

December 2013

ABSTRACT

Polarization Diversity in the Presence of Multipath Propagation

Grant T. Wagner
Department of Electrical and Computer Engineering
Master of Science

The possibility of polarization diversity using left and right hand circular polarization (LHCP and RHCP) in the presence of multipath propagation is examined. We show that there are differences in the received signal for LHCP and RHCP for a number of realistic scenarios. Because multipath propagation can produce different LHCP and RCHP signals, there exists the possibility for diversity improvement involving the two polarizations.

Keywords: polarization, diversity, MIMO, telemetry, multipath propagation

ACKNOWLEDGMENTS

I would like to thank my advisor, Dr. Michael Rice, for all of the help and guidance he has given me during my time at BYU. Without his help and patience this thesis would not have been possible. I would also like to thank all the other professors in the Electrical Engineering department who have taught me and helped me learn.

Table of Contents

List of Figures

Chapter 1

Introduction

Diversity techniques can be used to minimize the effects of multipath interference in wireless communication channels. Polarization is one characteristic of wireless signals that can be exploited for diversity gains. Airborne test articles at test ranges typically use dipole antennas mounted on the aircraft for telemetry transmission. This creates a signal with a linear polarization; a dipole mounted on the bottom of the fuselage of an aircraft flying straight and level produces a vertically polarized signal. As the aircraft maneuvers, the polarization changes. Because the receive antenna does not know the aircraft orientation, the receive antenna does not know the polarization of the received signal. Consequently, the receive antenna feed, equipped with vertical and horizontal dipole elements in a resonant cavity, is in general not aligned with the polarization of the received signal. For this reason, the receive antenna synthesizes a circularly polarized signal by combining its own vertical (V) and horizontal (H) components using an appropriate phase shift. The result is a receive system that is immune to the aircraft orientation. This thesis will examine left- and right-hand circular polarization (LHCP and RHCP) in aeronautical telemetry channels and whether they can be exploited for diversity gains in the test range environment.

In Chapter 2 a simple multipath model is used to derive expressions for the open circuit voltage phasors on the receivers V and H components. These two open circuit voltage phasors are used to synthesize LHCP and RHCP and model the received signal. Then the phasor frequencies are swept across bandwidths commonly used in aeronautical telemetry to create the frequency domain transfer function. If the LHCP and RHCP frequency domain transfer functions are different, then we conclude that the possibility of diversity improvement exists. The analysis shows that variations in the polarization due to maneuvers of the aircraft and ground bounce reflections create differences in the signal that have potential for diversity gains.

Chapter 3 compares the model derived in chapter 2 to real data collected from multipath channel sounding experiments conducted at Edwards Air Force Base, CA in 2011. This analysis shows close agreement between the model derived in Chapter 2 to the actual data.

Chapter 2

Theoretical Model

This chapter will examine the received signal in left- and right-hand circular polarization (LHCP and RHCP) in aeronautical telemetry channels using a simple multipath model and whether they can be exploited for diversity gains in the test range environment. We show that the variations in the polarization due to maneuvers of the aircraft and ground bounce reflections create differences in the signal that may possibly be exploited for diversity gains.

2.1 System Model

The system model used in this work is outlined in Figure 2.1. The key components are the transmitter (a "vertical" dipole mounted on the bottom of an aircraft), a receive antenna (a parabolic reflector tracking antenna), and a reflecting surface. The analysis will be carried out in the two coordinate systems shown. The (x, y, z) coordinate system, with unit-length vectors $\hat{\mathbf{x}}$, $\hat{\mathbf{y}}$, and $\hat{\mathbf{z}}$, is centered at the reflection point and aligned with the reflecting surface. The (x', y', z') coordinate system with unit-length vectors $\hat{\mathbf{x}}'$, $\hat{\mathbf{y}}'$, and $\hat{\mathbf{z}}'$, is centered at the receive antenna and aligned with the direction the antenna is pointing. We assume straight-and-level flight is parallel to the y-axis in the (x, y, z) coordinate system. Consequently, the (x', y', z') coordinate system is related to the (x, y, z) coordinate system via a rotation about the y-axis by the antenna elevation angle θ_e given by

$$\theta_e = \tan^{-1}\left(\frac{h_t - h_r}{R}\right). \tag{2.1}$$

The rays representing the line-of-sight and reflected components all lie in the $x - z$ plane in the (x, y, z) coordinate system. The line-of-sight plane wave along with the two plane waves constituting the reflected wave, are illustrated in Figure 2.1. Associated with each of these waves are electric and magnetic fields. The standard convention is used in defining these fields [1]. For the line-of-sight wave, the electric field $\mathbf{E}^L$ and the magnetic field $\mathbf{H}^L$ are represented by vectors

in a plane normal to the direction of propagation. For example, the line-of-sight wave propagates along the z'-axis in the (x', y', z') coordinate system. The electric field vector $\mathbf{E}^L$ is a vector aligned with the x'-axis and the magnetic field vector $\mathbf{H}^L$ is a vector aligned with the y'-axis. The electric-field vectors $\mathbf{E}^L$, $\mathbf{E}^I$, and $\mathbf{E}^R$, for the line-of-sight, indirect, and reflected waves, respectively, are shown in Figure 2.1.

The polarization state of the plane wave is defined as the unit-length vector coinciding with the electric field vector. This vector will be denoted $\hat{\mathbf{p}}$ in the discussion below. The polarization state of the transmitted wave is determined by the spatial orientation of the transmit dipole. With reference to Figure 2.1, the polarization states for the line-of-sight, indirect, and reflected waves are unit-length vectors $\hat{\mathbf{p}}^L$, $\hat{\mathbf{p}}^I$, and $\hat{\mathbf{p}}^R$ coinciding with the vectors $\mathbf{E}^L$, $\mathbf{E}^I$, and $\mathbf{E}^R$, respectively.

The transmit antenna is a "vertical" dipole mounted on the bottom of the aircraft at an altitude h_t AGL. The polarization state of the transmitted signal depends on the pitch ϕ_a of the aircraft. When $\phi_a = 0$, the polarization vector of the transmitted signal lies entirely in the $x - z$ plane of the (x, y, z) coordinate system. When $\phi_a \neq 0$, then there is a y-axis component to the polarization state.

The receive antenna is a parabolic reflector at a height h_r AGL. The receive antenna tracks the position of the airborne transmitter. At the antenna focal point, a resonant cavity is equipped with "cross" dipoles coinciding with the x' and z' axes as shown. For the purposes of this study, gain is less of a concern than polarization state of the received wavefronts. Consequently, we assume that for small angles off boresight, the reflector, resonant cavity, and cross-dipole structure may be replaced by a pair of dipoles at the origin of the (x', y', z') coordinate system as shown.

To model a common multipath environment at test ranges in the western USA, a simple 2-ray model is used as shown in Figure 2.1. This multipath reflection can be modeled as a single reflection off a flat, smooth surface [2]. This surface is commonly a dry lake bed at test ranges in the western USA [2] or ocean water at sea based test ranges [3]. The distances R, h_t, and h_r can be used to find the incident angle, θ_i, of the multipath reflection and the elevation angle θ_e The beamwidths of antennas used in aeronautical telemetry range from 3° to 6° [2] so only ground reflections with incident angles close to 90° will cause multipath interference.

We first determine equations for the two electric fields incident on the receive antenna feed, $\mathbf{E}^L$ and $\mathbf{E}^R$. Next, we calculate the open-circuit voltage induced in the *vertical* receive antenna

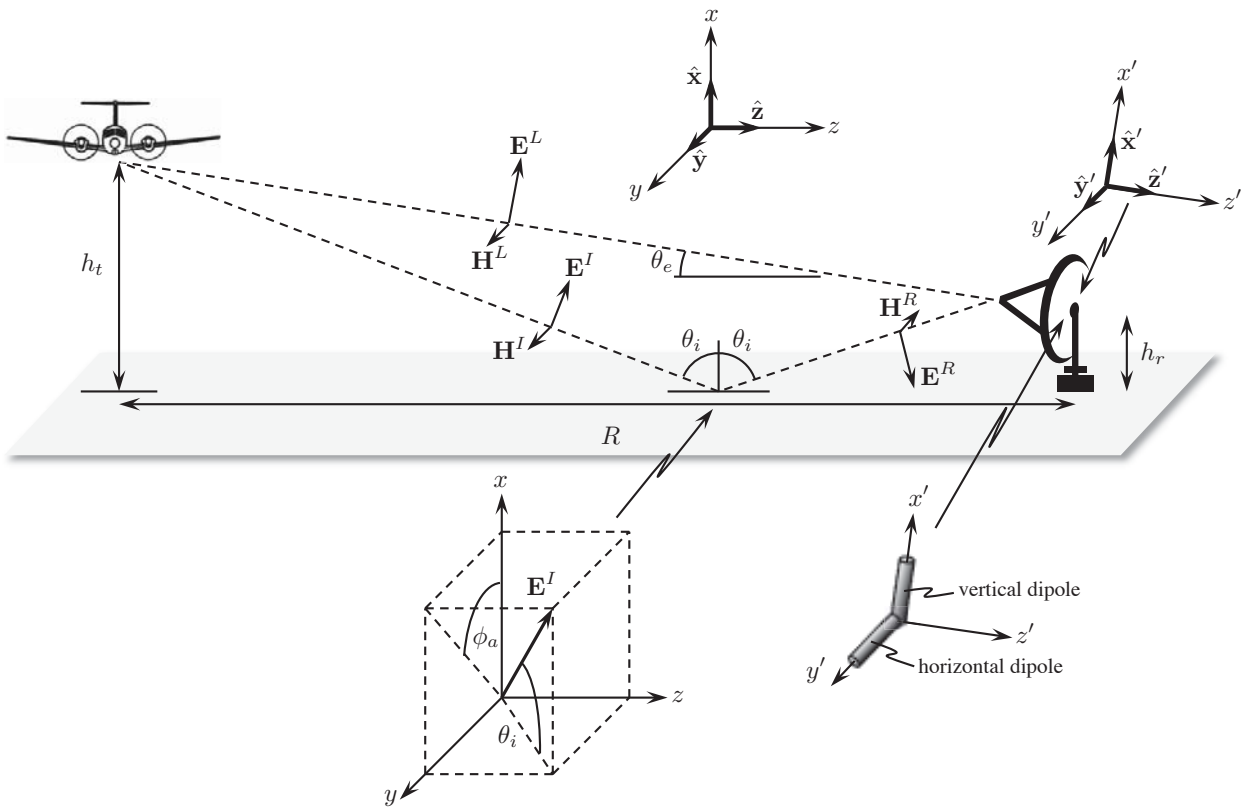

Figure 2.1: Geometry of single reflection telemetry channel.

feed due to $\mathbf{E}^L$ and $\mathbf{E}^R$. Then, we calculate the open-circuit voltage induced in the *horizontal* receive antenna feed due to $\mathbf{E}^L$ and $\mathbf{E}^R$. Finally, the voltages from the vertically and horizontally polarized components are combined to synthesize right- and left-hand circular polarizations. This result allows us to examine the potential for polarization diversity in a multipath environment.

2.2 Analysis

2.2.1 Line-of-sight Component

The line-of-sight wave can be represented as a uniform plane wave in the (x', y', z') coordinate system where $\hat{\mathbf{z}}'$ is in the direction of the line-of-sight propagation [1]. Thus in the (x', y', z') coordinate system

$$\mathbf{E}^L = E^L \left[\cos(\phi_a)\hat{\mathbf{x}}' + \sin(\phi_a)\hat{\mathbf{y}}'\right] e^{-j\mathbf{k}'_L \cdot \mathbf{r}'} = \tilde{\mathbf{E}}^L e^{-j\mathbf{k}'_L \cdot \mathbf{r}'} \tag{2.2}$$

where E^L is the intensity of the plane wave and ϕ_a is the aircraft pitch angle. The phase term involves the dot product of two vectors, $\mathbf{k}'_L$ and $\mathbf{r}'$. The vector $\mathbf{k}'_L$ is given by

$$\mathbf{k}'_L = \frac{2\pi}{\lambda}\hat{\mathbf{r}} \tag{2.3}$$

where λ is the wavelength and $\hat{\mathbf{r}}$ is a unit-length vector representing the direction of propagation in (x', y', z') coordinate system. The vector $\mathbf{r}'$ is a point in the (x', y', z') coordinate system representing the point in space where the wave is observed.

2.2.2 Specular Reflection Component

The physics of the reflecting wave are well understood. All the major results in this section are derived from [1]. The geometry of $\mathbf{E}^I$ is illustrated in Figure 2.1. Here, the incidence angle θ_i is a function of h_t, h_r and R. As before, ϕ_a is the aircraft pitch angle. The electric field corresponding to the indirect wave may be expressed in the (x, y, z) coordinate system as

$$\mathbf{E}^I = E^I \left[\sin(\theta_i)\cos(\phi_a)\hat{\mathbf{x}} + \sin(\theta_i)\sin(\phi_a)\hat{\mathbf{y}} + \cos(\theta_i)\hat{\mathbf{z}}\right] e^{-j\mathbf{k}_i\cdot\mathbf{r}} \tag{2.4}$$

where E^I is the intensity of the uniform plane wave, $\mathbf{r}$ is the observation point in the (x, y, z) coordinate system, and $\mathbf{k}_I$ is the vector representing the direction of propagation in (x, y, z) coordinate system. To compute the properties of the electric field corresponding to the reflected wave, we examine the vertical and horizontal components of $\mathbf{E}^I$ individually. To begin, we have

$$\mathbf{E}^I = \mathbf{E}^I_v + \mathbf{E}^I_h \tag{2.5}$$

where

$$\mathbf{E}^I_v = E^I \left[\sin(\theta_i)\cos(\phi_a)\hat{\mathbf{x}} + \cos(\theta_i)\hat{\mathbf{z}}\right] e^{-j\mathbf{k}_I\cdot\mathbf{r}}, \tag{2.6}$$

$$\mathbf{E}^I_h = E^I \sin(\theta_i)\sin(\phi_a)\hat{\mathbf{y}} e^{-j\mathbf{k}_I\cdot\mathbf{r}}. \tag{2.7}$$

The vector representing the electric field of the reflection may be written as

$$\mathbf{E}^R = \mathbf{E}_v^R + \mathbf{E}_h^R \tag{2.8}$$

where

$$\mathbf{E}_v^R = \Gamma_v E^I \left[-\sin(\theta_i)\cos(\phi_a)\hat{\mathbf{x}} + \cos(\theta_i)\hat{\mathbf{z}} \right] e^{-j\mathbf{k}_R\cdot\mathbf{r}}, \tag{2.9}$$

$$\mathbf{E}_h^R = \Gamma_h E^I \left(\sin(\theta_i)\sin(\phi_a)\hat{\mathbf{y}} \right) e^{-j\mathbf{k}_R\cdot\mathbf{r}}. \tag{2.10}$$

In Equations (2.9) and (2.10), Γ_v and Γ_h are the reflection coefficients given by [1]

$$\Gamma_h = \frac{-\cos(\theta_i) + \sqrt{\frac{\epsilon_0}{\epsilon_1}}\sqrt{1 - \frac{\epsilon_0}{\epsilon_1}\sin^2(\theta_i)}}{\cos(\theta_i) + \sqrt{\frac{\epsilon_0}{\epsilon_1}}\sqrt{1 - \frac{\epsilon_0}{\epsilon_1}\sin^2(\theta_i)}}, \tag{2.11}$$

$$\Gamma_v = \frac{\cos(\theta_i) - \sqrt{\frac{\epsilon_1}{\epsilon_0}}\sqrt{1 - \frac{\epsilon_0}{\epsilon_1}\sin^2(\theta_i)}}{\cos(\theta_i) + \sqrt{\frac{\epsilon_1}{\epsilon_0}}\sqrt{1 - \frac{\epsilon_0}{\epsilon_1}\sin^2(\theta_i)}} \tag{2.12}$$

where ϵ_0 and ϵ_1 are the the permittivity of free space and of the reflecting media, respectively.[1] Combining (2.9) and (2.10) gives

$$\mathbf{E}^R = E^I \left[-\Gamma_v \sin(\theta_i)\cos(\phi_a)\hat{\mathbf{x}} + \Gamma_h \sin(\theta_i)\sin(\phi_a)\hat{\mathbf{y}} + \Gamma_v \cos(\theta_i)\hat{\mathbf{z}} \right] e^{-j\mathbf{k}_R\cdot\mathbf{r}}. \tag{2.13}$$

In the (x', y', z') coordinate system, $\mathbf{E}^R$ is

$$\mathbf{E}^R = E^I \left[-\Gamma_v \cos(\theta_r)\cos(\phi_a)\hat{\mathbf{x}}' + \Gamma_v \sin(\theta_r)\hat{\mathbf{z}} + \Gamma_h \cos(\theta_r)\sin(\phi_a)\hat{\mathbf{y}}' \right] e^{-jk\Delta\rho} e^{-j\mathbf{k}_R\cdot\mathbf{r}} \tag{2.14}$$

$$= \tilde{\mathbf{E}}^R e^{-j\mathbf{k}_R\cdot\mathbf{r}} \tag{2.15}$$

[1] The free space permittivity is $\epsilon_0 = 8.85 \times 10^{-12}$ F/m. For dry earth and sea water the permittivities are, respectively,

$$\epsilon_1 = 3\epsilon_0 + \frac{3 \times 10^{-4}}{j\omega_c} \qquad \epsilon_1 = 81\epsilon_0 + \frac{5}{j\omega_c}$$

where ω_c is the RF carrier frequency in rads/s.

where $\Delta\rho$ is the difference between the length of the line-of-sight path and the length of the path taken by the indirect and reflected rays, and θ_r is the angle between the line-of-sight ray and the reflected ray and is given by

$$\theta_r = (90 - \theta_i) + \tan^{-1}\left(\frac{h_t - h_r}{R}\right). \tag{2.16}$$

2.2.3 Open-circuit Voltage Phasors

The relationship between an arbitrary incident electric field $\mathbf{E}^i$ and the open circuit voltage V_{oc} at the antenna terminals is [4]

$$V_{\text{oc}} = \frac{1}{I_0}\frac{4\pi j\rho e^{jk\rho}}{\omega_c \mu} E^i \hat{\mathbf{p}} \cdot \mathbf{E}^t(\mathbf{r}) \tag{2.17}$$

where I_0 is the corresponding current in the antenna element, ρ is the distance between the antenna element and electric field, $k = 2\pi/\lambda$ is the wave number, ω_c is the carrier frequency in rads/s, μ is the permeability of the propagation medium, E^i is the electric field intensity, $\hat{\mathbf{p}}$ is the polarization vector for the electric field (i.e. $\hat{\mathbf{p}}$ is a unit-length vector coinciding with $\mathbf{E}^i$), and $\mathbf{E}^t(\mathbf{r})$ is the far-field electric field at location $\mathbf{r}$. For the line-of-sight field, $E^i\hat{\mathbf{p}}$ in (2.17) is given by $\tilde{\mathbf{E}}^L$ in (2.2) whereas for the reflected wave $E^i\hat{\mathbf{p}}$ in (2.17) is given by $\tilde{\mathbf{E}}^R$ in (2.15).

The term $\mathbf{E}^t(\mathbf{r})$ may be expressed in terms of the current density $\mathbf{J}(\mathbf{r}')$ at location $\mathbf{r}'$ in the antenna element. The corresponding current moment is

$$\mathbf{N}(\mathbf{r}) = \int e^{jk\mathbf{r}\cdot\mathbf{r}'}\mathbf{J}(\mathbf{r}')d\mathbf{r}' \tag{2.18}$$

where the integral is over the antenna element volume. $\mathbf{E}^t(\mathbf{r})$ may be expressed as [4]

$$\mathbf{E}^t(\mathbf{r}) = -\frac{j\omega_c\mu e^{-jk\rho}}{4\pi\rho}\left(\mathbf{N}(\mathbf{r}) - \hat{\mathbf{r}}\left[\hat{\mathbf{r}}\cdot\mathbf{N}(\mathbf{r})\right]\right) \tag{2.19}$$

where $\hat{\mathbf{r}}$ is a unit-length version of the vector $\mathbf{r}$ between the antenna element and the point where the electric field is observed. This expression may be simplified by converting to the spherical coordinate system (ρ, θ, ϕ) with unit-length basis vectors $\hat{\boldsymbol{\rho}}$, $\hat{\boldsymbol{\theta}}$, $\hat{\boldsymbol{\phi}}$. Now, the current moment may

be expressed as

$$\mathbf{N}(\mathbf{r}) = N_\rho \hat{\boldsymbol{\rho}} + N_\theta \hat{\boldsymbol{\theta}} + N_\phi \hat{\boldsymbol{\phi}} \tag{2.20}$$

and the vector $\mathbf{r}$ is simply $\mathbf{r} = \rho\hat{\boldsymbol{\rho}}$ and $\hat{\mathbf{r}} = \hat{\boldsymbol{\rho}}$. In the spherical coordinate system, the dot product is

$$\hat{\mathbf{r}} \cdot \mathbf{N}(\mathbf{r}) = \hat{\boldsymbol{\rho}} \cdot \left[N_\rho \hat{\boldsymbol{\rho}} + N_\theta \hat{\boldsymbol{\theta}} + N_\phi \hat{\boldsymbol{\phi}} \right] = N_\rho \tag{2.21}$$

so that the term inside the parenthesis in (2.19) becomes

$$\mathbf{N}(\mathbf{r}) - \hat{\mathbf{r}} \left[\hat{\mathbf{r}} \cdot \mathbf{N}(\mathbf{r}) \right] = N_\rho \hat{\boldsymbol{\rho}} + N_\theta \hat{\boldsymbol{\theta}} + N_\phi \hat{\boldsymbol{\phi}} - N_\rho \hat{\boldsymbol{\rho}} = N_\theta \hat{\boldsymbol{\theta}} + N_\phi \hat{\boldsymbol{\phi}}. \tag{2.22}$$

Consequently, the far-field electric field may be expressed as

$$\mathbf{E}^t(\mathbf{r}) = -\frac{j\omega_c \mu e^{-jk\rho}}{4\pi\rho} \left(N_\theta \hat{\boldsymbol{\theta}} + N_\phi \hat{\boldsymbol{\phi}} \right). \tag{2.23}$$

This term is a function of both the observation point for the electric field and the current density of the antenna element. Substituting (2.23) into (2.17) and simplifying gives

$$V_{\text{oc}} = \frac{1}{I_0} E^i \hat{\mathbf{p}} \cdot \left(N_\theta \hat{\boldsymbol{\theta}} + N_\phi \hat{\boldsymbol{\phi}} \right). \tag{2.24}$$

2.2.4 Vertical Polarization

For a vertically oriented dipole such as that shown in Figure 2.1, the current density is

$$\mathbf{J}_v(\mathbf{r}) = I_0 \ell \hat{\mathbf{x}}' \delta(\mathbf{r}) \tag{2.25}$$

where $\delta(\mathbf{r})$ is the three-dimensional Dirac impulse function that places the current source at the origin of the coordinate system and ℓ is the length of the vertical dipole serving as the antenna element. The vector current moment is

$$\mathbf{N}_v(\mathbf{r}) = I_0 \ell \hat{\mathbf{x}}' = \underbrace{I_0 \ell \sin(\theta)\cos(\phi)}_{N_\rho} \hat{\boldsymbol{\rho}} + \underbrace{I_0 \ell \cos(\theta)\cos(\phi)}_{N_\theta} \hat{\boldsymbol{\theta}} - \underbrace{I_0 \ell \sin(\phi)}_{N_\phi} \hat{\boldsymbol{\phi}} \tag{2.26}$$

from which the open-circuit voltage is

$$V_{\text{oc}} = E^i \hat{\mathbf{p}} \cdot \left(\ell \cos(\theta)\cos(\phi)\hat{\boldsymbol{\theta}} - \ell \sin(\phi)\hat{\boldsymbol{\phi}} \right) \tag{2.27}$$

$$= E^i \hat{\mathbf{p}} \cdot \ell \Big(\left[\cos^2(\theta)\cos^2(\phi) + \sin^2(\phi)\right] \hat{\mathbf{x}}' + \left[\cos^2(\theta)\cos(\phi)\sin(\phi) - \cos(\phi)\sin(\phi)\right] \hat{\mathbf{y}}' - \left[\cos(\theta)\sin(\theta)\cos(\phi)\right] \hat{\mathbf{z}}' \Big). \tag{2.28}$$

For the line-of-sight electric field, $E^i\hat{\mathbf{p}} = \tilde{\mathbf{E}}^L$ from (2.2) and $\theta = \phi = 0$, so we have

$$V_{\text{oc}}^{L,v} = E^L \left[\cos(\phi_a)\hat{\mathbf{x}}' + \sin(\phi_a)\hat{\mathbf{y}} \right] \cdot \ell\hat{\mathbf{x}}' = E^L \ell \cos(\phi_a). \tag{2.29}$$

For the reflected electric field $E^i\hat{\mathbf{p}} = \tilde{\mathbf{E}}^R$ from (2.15) and $\theta = \theta_r$, $\phi = 0$, so we have

$$V_{\text{oc}}^{R,v} = E^i \left[-\Gamma_v \cos(\theta_r)\cos(\phi_a)\hat{\mathbf{x}}' + \Gamma_h \cos(\theta_r)\sin(\phi_a)\hat{\mathbf{y}}' + \Gamma_v \sin(\theta_r)\hat{\mathbf{z}}' \right] e^{-jk\Delta\rho} \cdot \ell \left[\cos^2(\theta_r)\hat{\mathbf{x}}' - \cos(\theta_r)\sin(\theta_r)\hat{\mathbf{z}}' \right]$$

$$= -E^i \ell \Gamma_v \left[\cos^3(\theta_r)\cos(\phi_a) + \cos(\theta_r)\sin^2(\theta_r) \right] e^{-jk\Delta\rho}. \tag{2.30}$$

The open-circuit voltage at the vertical dipole terminals is

$$V_{\text{oc}}^v = V_{\text{oc}}^{L,v} + V_{\text{oc}}^{R,v} = E^L \ell \cos(\phi_a) - E^i \ell \Gamma_v \left[\cos^3(\theta_r)\cos(\phi_a) + \cos(\theta_r)\sin^2(\theta_r) \right] e^{-jk\Delta\rho}. \tag{2.31}$$

2.2.5 Horizontal Polarization

For a horizontally oriented dipole such as that shown in Figure 2.1, the current density is

$$\mathbf{J}_h(\mathbf{r}) = I_0 \ell \hat{\mathbf{y}}' \delta(\mathbf{r}) \tag{2.32}$$

where $\delta(\mathbf{r})$ is the three-dimensional Dirac impulse function that places the current source at the origin of the coordinate system and ℓ is the length of the vertical dipole serving as the antenna

element. The vector current moment is

$$\mathbf{N}_h(\mathbf{r}) = I_0\ell\hat{\mathbf{y}}' = \underbrace{I_0\ell\sin(\theta)\sin(\phi)}_{N_\rho}\hat{\boldsymbol{\rho}} + \underbrace{I_0\ell\cos(\theta)\sin(\phi)}_{N_\theta}\hat{\boldsymbol{\theta}} + \underbrace{I_0\ell\cos(\phi)}_{N_\phi}\hat{\boldsymbol{\phi}} \tag{2.33}$$

from which the open-circuit voltage is

$$\begin{aligned} V_{\text{oc}} &= E^i\hat{\mathbf{p}}\cdot\Big(\ell\cos(\theta)\sin(\phi)\hat{\boldsymbol{\theta}} - \ell\cos(\phi)\hat{\boldsymbol{\phi}}\Big) &(2.34)\\ &= E^i\hat{\mathbf{p}}\cdot\ell\Big(\left[\cos^2(\theta)\cos(\phi)\sin(\phi) - \cos(\phi)\sin(\phi)\right]\hat{\mathbf{x}}' \\ &\qquad + \left[\cos^2(\theta)\sin^2(\phi) + \cos^2(\phi)\right]\hat{\mathbf{y}}' \\ &\qquad - \left[\cos(\theta)\sin(\theta)\sin(\phi)\right]\hat{\mathbf{z}}'\Big). &(2.35)\end{aligned}$$

For the line-of-sight electric field, $E^i\hat{\mathbf{p}} = \tilde{\mathbf{E}}^L$ from (2.2) and $\theta = \phi = 0$, so we have

$$V_{\text{oc}}^{L,h} = E^L\Big[\cos(\phi_a)\hat{\mathbf{x}}' + \sin(\phi_a)\hat{\mathbf{y}}\Big]\cdot\ell\hat{\mathbf{y}}' = E^L\ell\sin(\phi_a). \tag{2.36}$$

For the reflected electric field $E^i\hat{\mathbf{p}} = \tilde{\mathbf{E}}^R$ from (2.15) and $\theta = \theta_r$, $\phi = 0$, so we have

$$\begin{aligned} V_{\text{oc}}^{R,h} &= E^i\Big[-\Gamma_v\cos(\theta_r)\cos(\phi_a)\hat{\mathbf{x}}' + \Gamma_h\cos(\theta_r)\sin(\phi_a)\hat{\mathbf{y}}' + \Gamma_v\sin(\theta_r)\hat{\mathbf{z}}'\Big]\,e^{-jk\Delta\rho}\cdot\ell\hat{\mathbf{y}}' \\ &= -E^i\ell\Gamma_h\cos(\theta_r)\sin(\phi_a)e^{-jk\Delta\rho}. &(2.37)\end{aligned}$$

The open-circuit voltage at vertical dipole terminals is

$$V_{\text{oc}}^h = V_{\text{oc}}^{L,h} + V_{\text{oc}}^{R,h} = E^L\ell\sin(\phi_a) + E^i\ell\Gamma_h\cos(\theta_r)\sin(\phi_a)e^{-jk\Delta\rho}. \tag{2.38}$$

The open-circuit voltages induced in the vertical and horizontal receive antenna elements due to $\mathbf{E}^L$ and $\mathbf{E}^R$ are given by

$$V_{\text{oc}}^{v} = E^{L}\ell\cos(\phi_a) - E^{I}\ell\Gamma_v\left[\cos^3(\theta_r)\cos(\phi_a) + \cos(\theta_r)\sin^2(\theta_r)\right]e^{-jk\Delta\rho}, \tag{2.39}$$

$$V_{\text{oc}}^{h} = E^{L}\ell\sin(\phi_a) + E^{I}\ell\Gamma_h\cos(\theta_r)\sin(\phi_a)e^{-jk\Delta\rho} \tag{2.40}$$

where ℓ is the length of the vertical and horizontal dipole elements.

2.2.6 LHCP and RHCP Voltage Phasors

Most antenna feeds used in aeronautical telemetry synthesize LHCP and RHCP signals using the voltages from the vertical and horizontal dipoles. The LHCP and RHCP open-circuit voltages are

$$V_{\text{oc}}^{\text{LHCP}} = V_{\text{oc}}^{v} + jV_{\text{oc}}^{h}, \tag{2.41}$$

$$V_{\text{oc}}^{\text{RHCP}} = V_{\text{oc}}^{v} - jV_{\text{oc}}^{h}. \tag{2.42}$$

The LHCP and RHCP open circuit voltages can be different. In this case there is a possibility for diversity improvement in the presence of multipath fading. The amount of diversity improvement depends on how different $V_{\text{oc}}^{\text{RHCP}}$ and $V_{\text{oc}}^{\text{LHCP}}$ are. The differences in two realistic scenarios are quantified in the next section.

2.3 Numerical Results

Here, $V_{\text{oc}}^{\text{LHCP}}$ and $V_{\text{oc}}^{\text{RHCP}}$ are evaluated in two realistic scenarios: an over-the-earth scenario motivated by the setting at Edwards AFB and an over-the-ocean scenario motivated by the setting at Pt. Mugu NAWC. In both cases the incidence angle θ_i is very close to 90°. Consequently, θ_r is small and we may safely assume the field intensities for the line-of-sight wave and the indirect wave, E^L and E^I in (2.39) and (2.40) are the same. Furthermore, we set $E^L\ell = E^I\ell = 1$ to normalize the results.

2.3.1 Edwards AFB Setting

The scenario explored in this section is motivated by the Cords Road flight corridor near Edwards AFB. The Cords Road flight corridor is an east-west flight path illustrated in Figure 2.2. Here the aircraft is at the point shown on the Cords Road flight path at an altitude of $5000'$ AMSL. The receiver is Building 4790 located on a small hill top at an altitude of $2966'$ AMSL. The reflecting surface is at an altitude of $2300'$ AMSL.

Figure 2.3 plots the magnitude and phase of the RCHP and LHCP open circuit voltage phasors as a function of the aircraft pitch angle ϕ_a. The carrier frequency is 1485.5, the center of lower L-band. This plot shows that when $\phi_a = 0$, the LHCP and RHCP are the same. This is the expected result because there is no electric field aligned with the horizontal dipole in receive antenna. As the pitch angle ϕ_a increases, the LHCP and RHCP phasors become more different.

Figure 2.4 plots the magnitude and phase of the LHCP and RHCP open circuit voltage phasors across the L-band frequencies for a fixed pitch angle $\phi_a = 10^\circ$. The frequency response displays the characteristic lobing associated with a strong specular reflection [2]. The interesting feature here is that the nulls for the LHCP and RHCP channels occur at different frequencies. This opens up the possibility that some sort of selection diversity could improve performance in this scenario, but this is a topic for another paper.

2.3.2 Pt. Mugu Setting

The scenario explored in this section is motivated by the sea range in the Pacific Ocean near Pt. Mugu NAWC. The main telemetry receiving site is located at Laguna Peak at an elevation of 434 m AMSL as shown in Figure 2.5. We assume the transmitter is a missile launched from the surface and airborne over San Nicolas Island at an altitude of 1000 m AMSL. (The assumption of a single vertical dipole mounted under the aircraft is stretched here, but we can still observe some useful general trends.) Because most missile tests are conducted in S-Band (2200–2290 MHz), we use frequencies in S-Band to evaluate the LHCP and RHCP outputs.

Figure 2.6 plots the magnitude and phase of the LHCP and RHCP open circuit voltage phasors as a function of the aircraft pitch angle ϕ_a. The carrier frequency is 2245 MHz, the center of lower S-band. As before, when $\phi_a = 0$ LHCP and RHCP coincide, but quickly diverge as ϕ_a

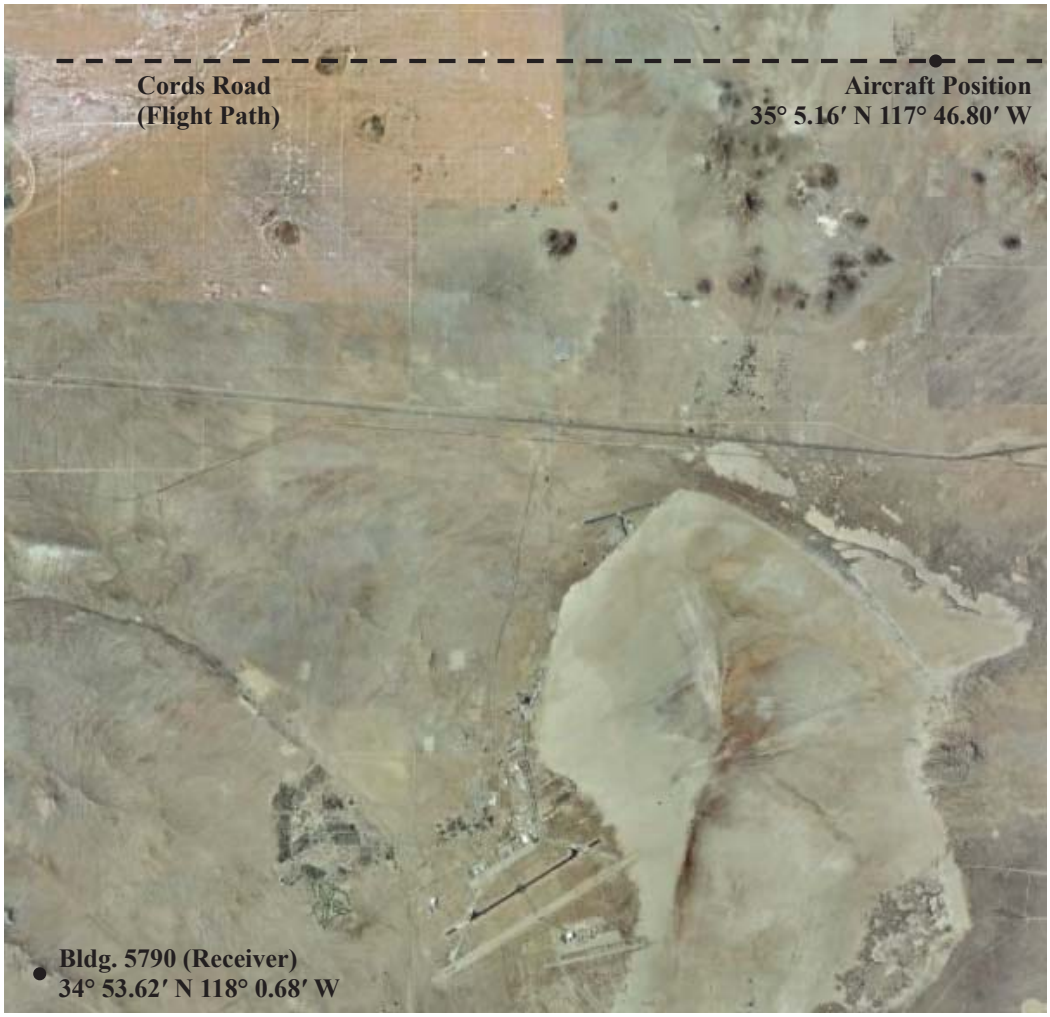

Figure 2.2: A map showing the positions used to define the 2-ray channel multipath channel scenario for Edwards AFB.

increases. LHCP and RHCP become different more quickly with increasing ϕ_a at S-band than at L-band because the wavelength is shorter at S-band.

Figure 2.7 plots the the magnitude and phase of the LHCP and RHCP open circuit voltage phasors as a function of frequency for a fixed pitch angle $\phi_a = 30°$. Again, we observe the characteristic lobing on both LHCP and RHCP but with the nulls at different frequencies. This shows that at most frequencies across S-band, the LHCP and RHCP signals are different, and this opens the possibility to performance improvement through polarization diversity.

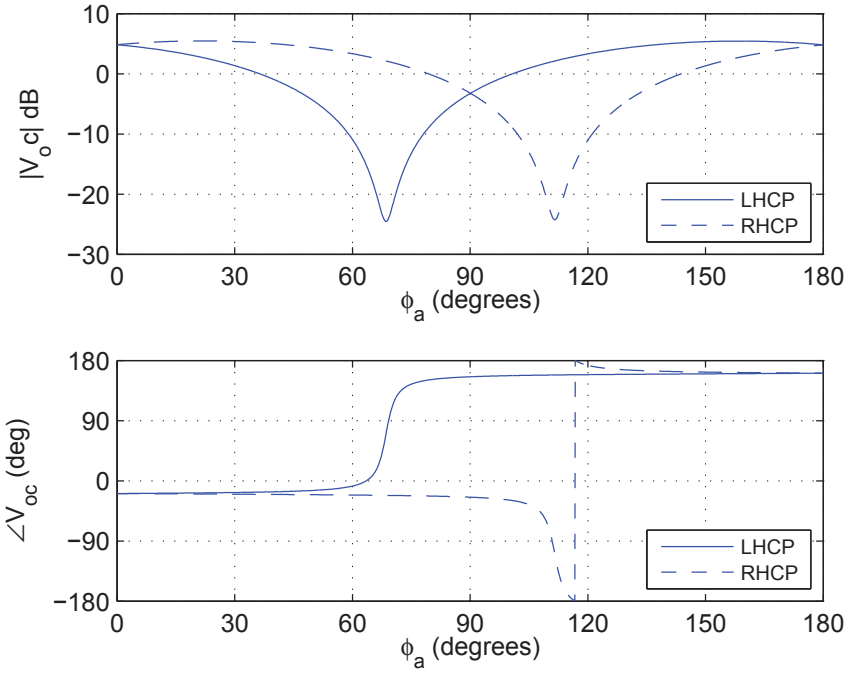

Figure 2.3: The open circuit voltage phasors corresponding to LHCP and RHCP as a function of the pitch angle ϕ_a for $f_c = 1485.5$ MHz and for the geometry summarized in Figure 2.2.

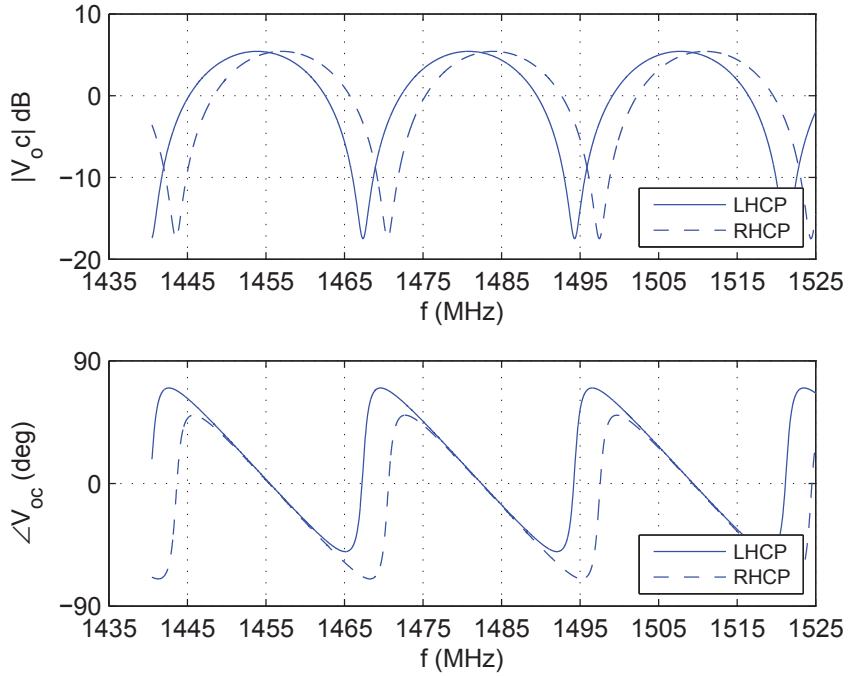

Figure 2.4: The open circuit voltage corresponding to LHCP and RHCP as a function of frequency (over lower L band) for a pitch angle $\phi_a = 10^\circ$ and for the geometry summarized in Figure 2.2.

Figure 2.5: A map showing the positions used to define the 2-ray channel multipath channel scenario for Pt. Mugu NAWC.

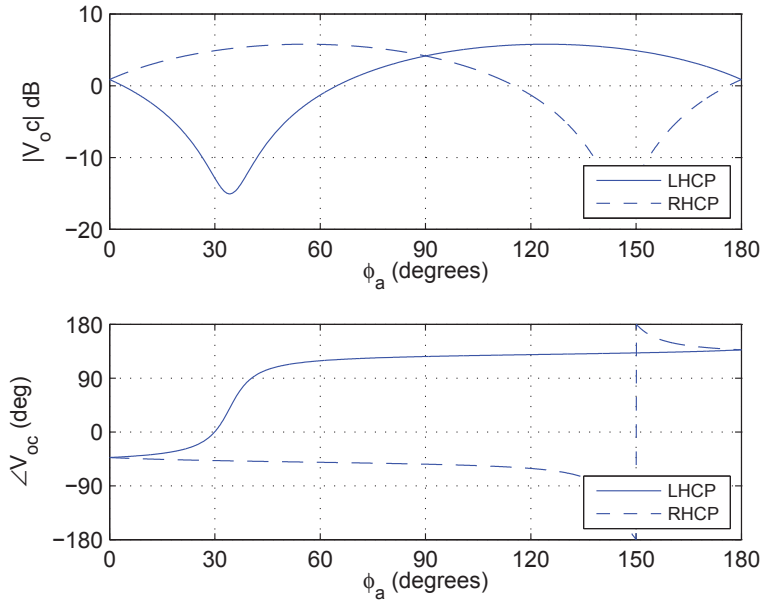

Figure 2.6: The open circuit voltage phasors corresponding to LHCP and RHCP as a function of the pitch angle ϕ_a for $f_c = 2245$ MHz and for the geometry summarized in Figure 2.5.

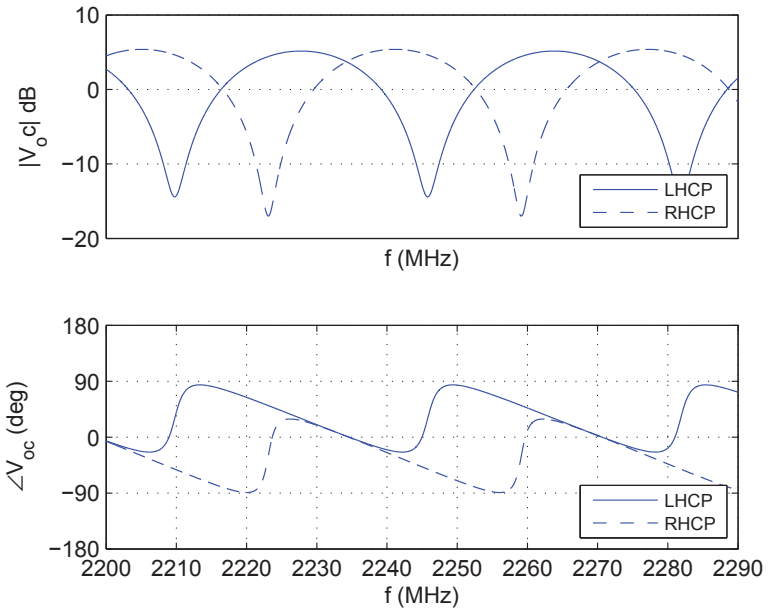

Figure 2.7: The open circuit voltage corresponding to LHCP and RHCP as a function of frequency (over S-band) for a pitch angle $\phi_a = 30^\circ$ and for the geometry summarized in Figure 2.5.

Chapter 3

Data Comparisons

This chapter compares theoretical predictions of frequency responses using the model laid out in the previous chapter to actual data collected from channel sounding experiments at Edwards Air Force Base, CA on the 3 February 2011. Details of the experiment can be found in [5] and [6].

3.1 Experimental Configuration

The channel sounding experiment airborne platform was a C-12 aircraft with 3 transmit antennas equipped to it as shown in Figure 3.1. The sounding signal was switched between the three transmit antennas using an RF switch. The connector supplying the power to transmit antenna three came loose before any of the test flights so no sounding signal was transmitted from antenna three. The channel sounding signal was centered at 1824.5 MHz (in upper L-band) and occupied 50 MHz of bandwidth.

The ground station configuration consisted of three physical antennas shown in Figure 3.2 set up at building 4795 at 34.9707° N, 117.9313° W, 792.45 m AMSL. Antennas 1 and 2 were derived from the two available polarizations output from the feed of a 5-meter parabolic reflector. Antennas 3 and 4 were not used in this analysis. Only data from antennas 1 and 2 were used because they differ only in their polarizations. Antenna 1 is RHCP and antenna 2 is LHCP.

The RF switch applied each input to the receiver one at a time and in synchronism with the transmitter switching. The relationship between the transmitter and receiver switching is shown in Figure 3.3.

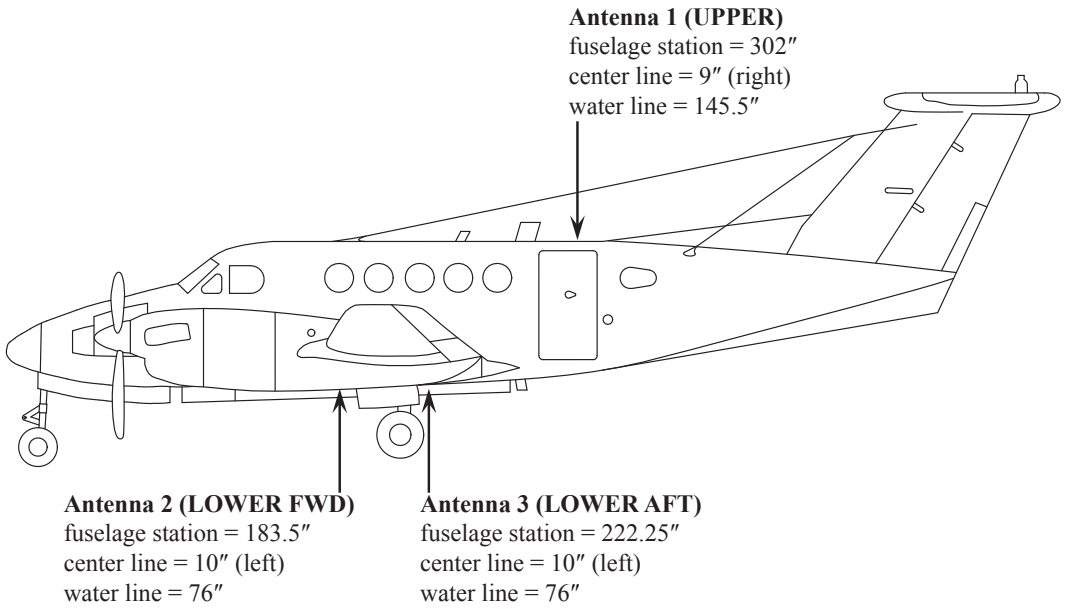

Figure 3.1: Airborne platform

3.2 Results

Two multipath events were identified from the experimental data acquired at Edwards AFB. The geometry at these locations was applied to the theoretical predictions made in the previous chapter and compared to the actual data acquired at these locations.

The first event was on the Cords Road flight corridor at $35.085°$ N, $117.0702°$ W, 1502.8 m AMSL (see Figure 3.4). The reflecting surface is at an altitude of $2300'$ AMSL and and a polarization angle of $2°$ was used. Figure 3.5 shows the predictions using the model described in Chapter 2. Figures 3.6 and 3.7 show the actual data received from transmitters 1 and 2 respectively.

The second event was on the Black Mt. flight corridor at $35.201°$ N, $117.2801°$ W, 1501.8 m AMSL (see Figure 3.8). The reflecting surface is at an altitude of $2300'$ AMSL and a polarization angle of $2°$ was used. Figure 3.9 shows the predictions using the model described in Chapter 2. Figures 3.10 and 3.11 show the actual data received from transmitters 1 and 2 respectively.

Figure 3.2: The view at Building 4795 showing the relative positions of the three physical antennas. Antenna 1/2 (the only one used in this analysis) is on the far right

In both events, we see many similarities between the actual data and the theoretical results. The frequency of the interference is not the exact same but these differences can be due to many things including errors in the exact location of the plane. It could also be due to any modeling errors such as the assumption of a smooth, flat reflecting surface with a precisely known reflection coefficient. Despite these simplifications in the model, there is close agreement between the model and experimental data.

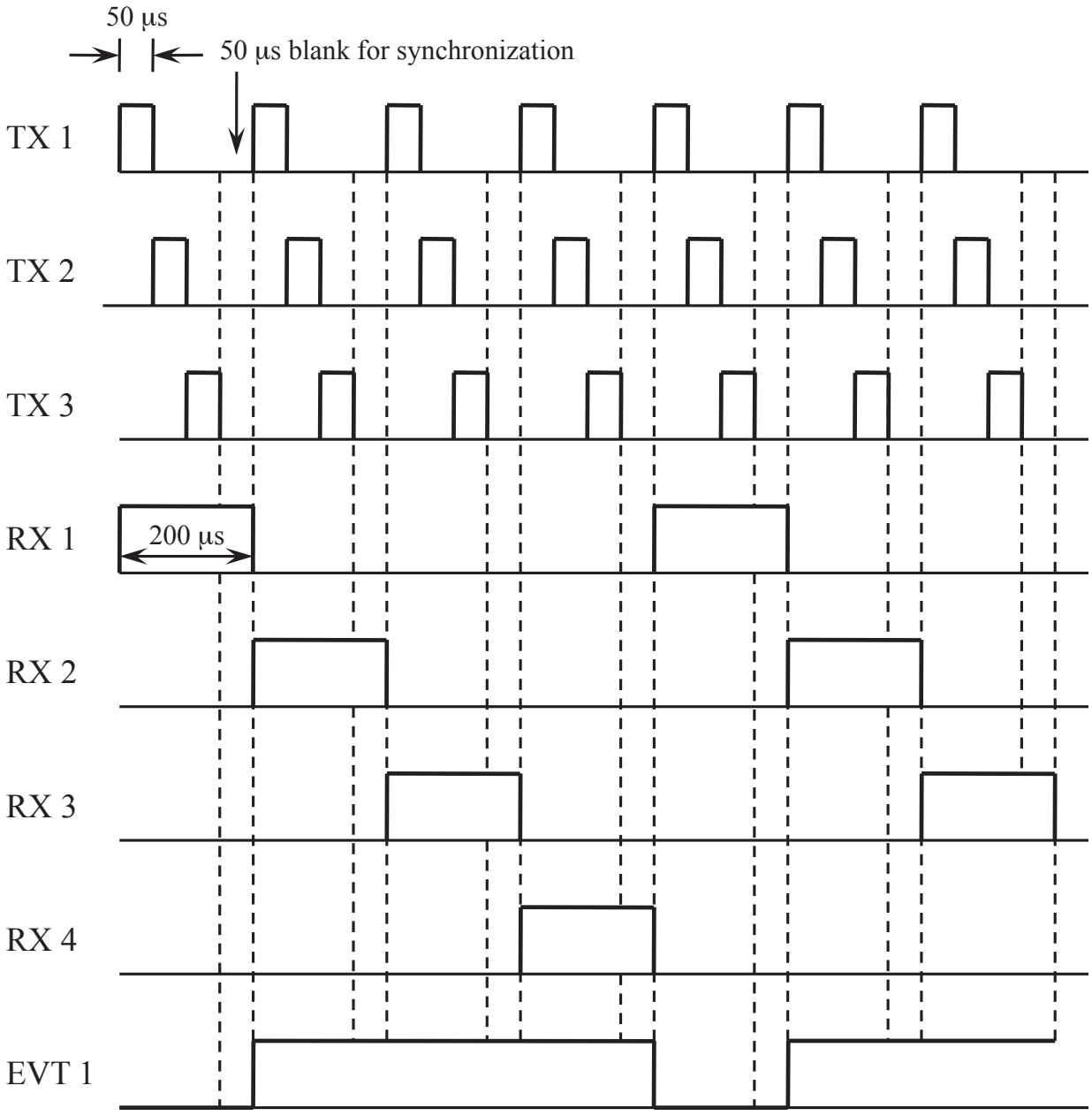

Figure 3.3: Switch control for transmitter are receiver.

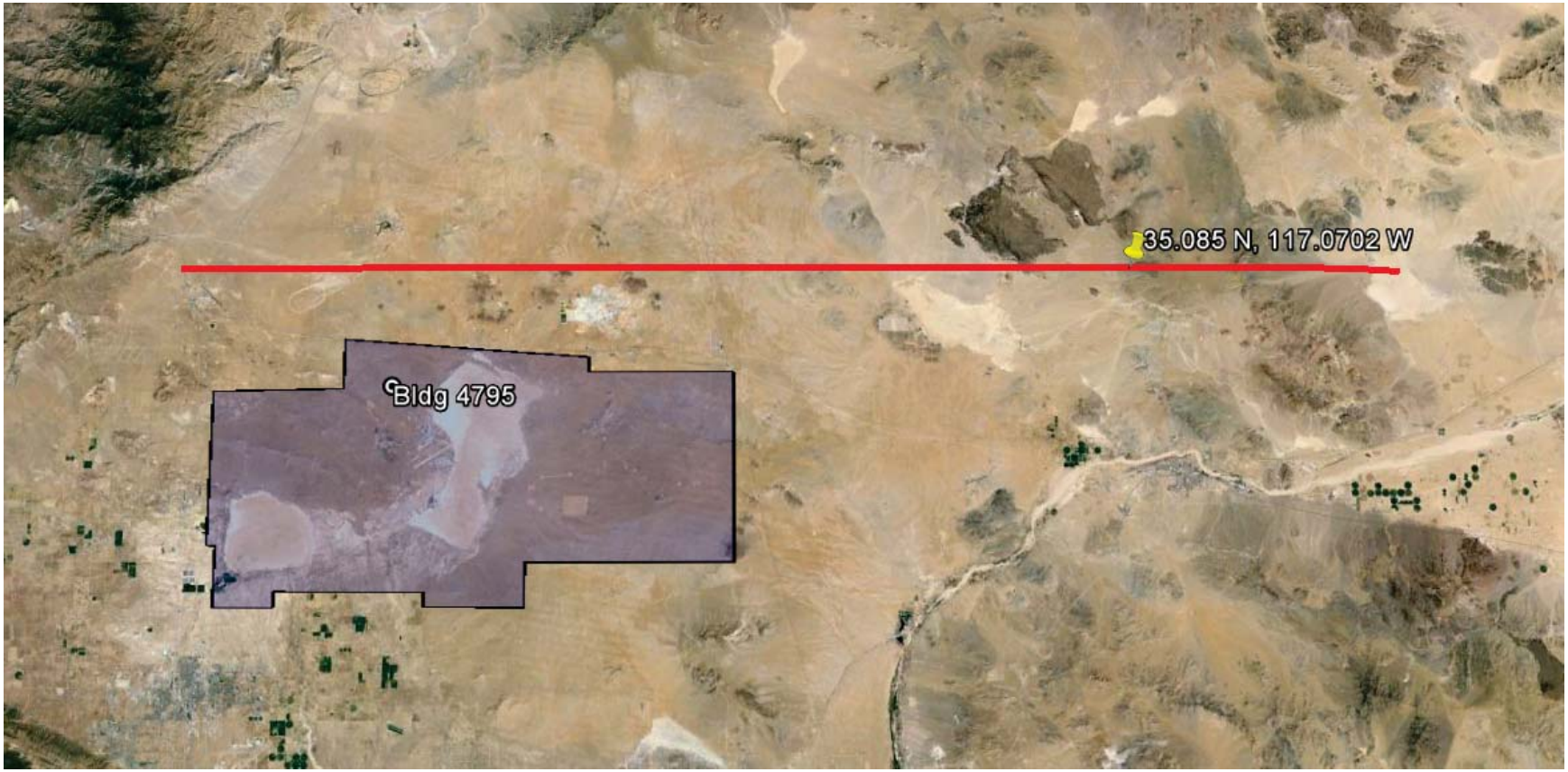

Figure 3.4: A map showing the positions of the transmitters and receivers during the multipath event on the Cords Road Corridor at Edwards AFB.

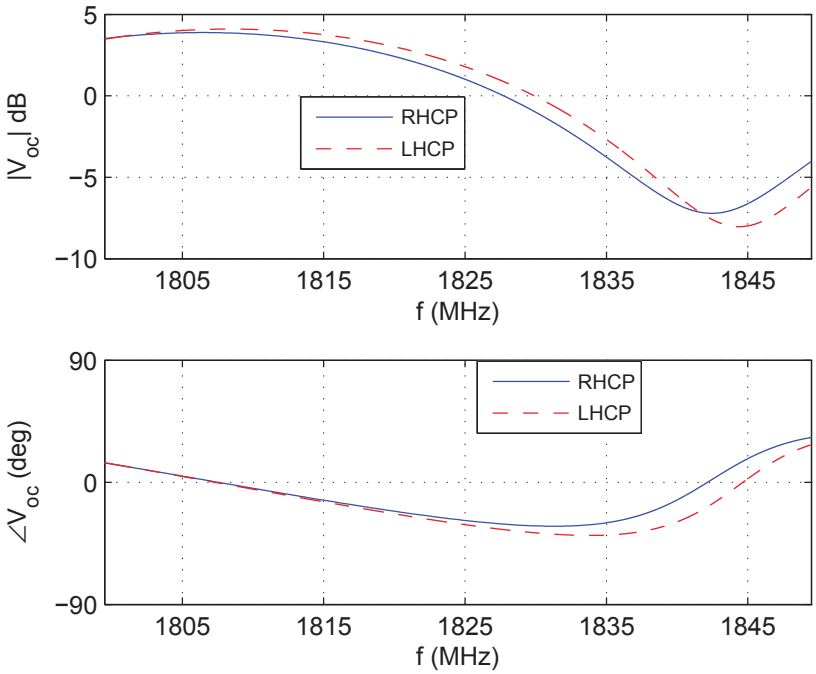

Figure 3.5: The simulated frequency response for the event shown in Figure 3.4.

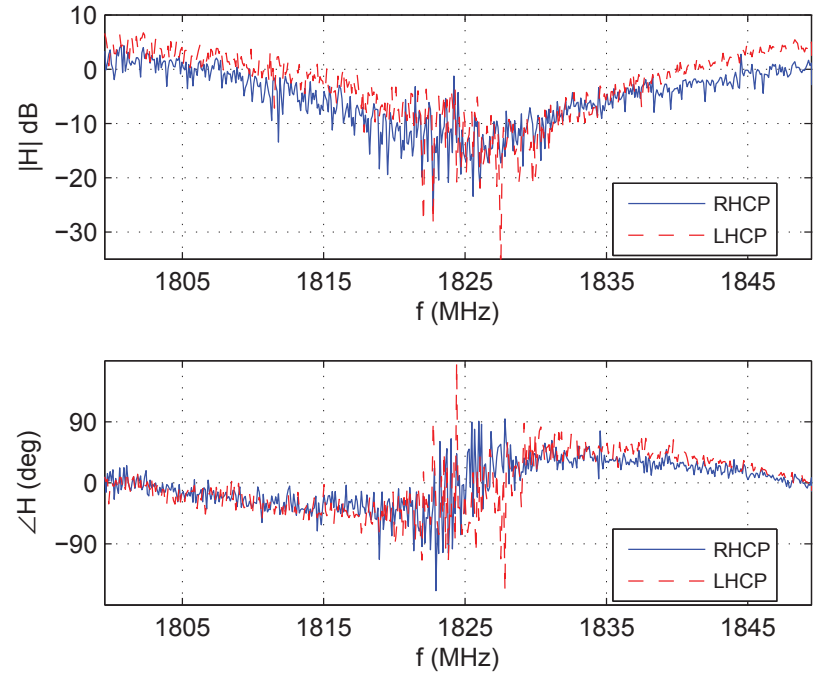

Figure 3.6: The frequency response from transmitter 1 from the channel sounding experiment during the event shown in Figure 3.4

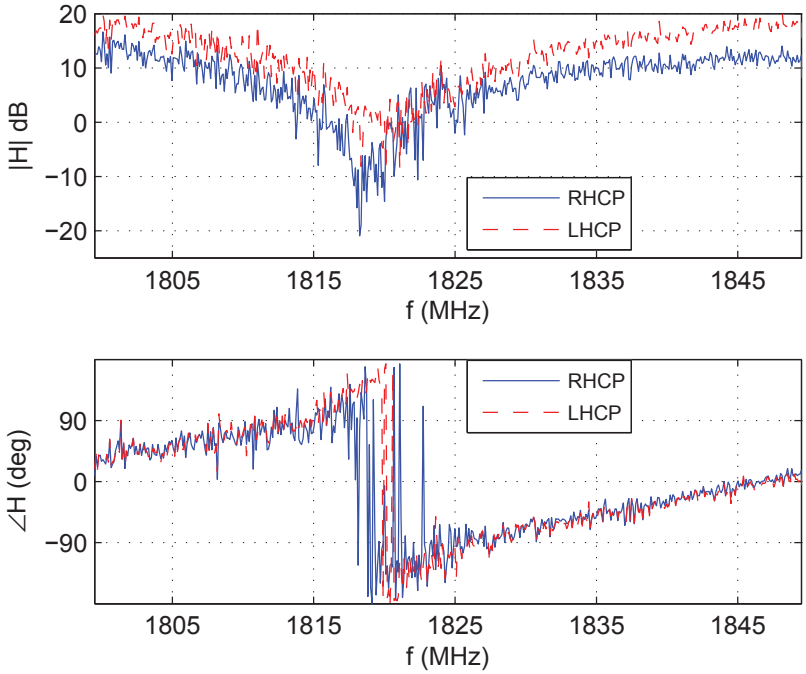

Figure 3.7: The frequency response from transmitter 2 from the channel sounding experiment during the event shown in Figure 3.4.

Figure 3.8: A map showing the positions of the transmitters and receivers during the multipath event on the Black Mountain Corridor at Edwards AFB.

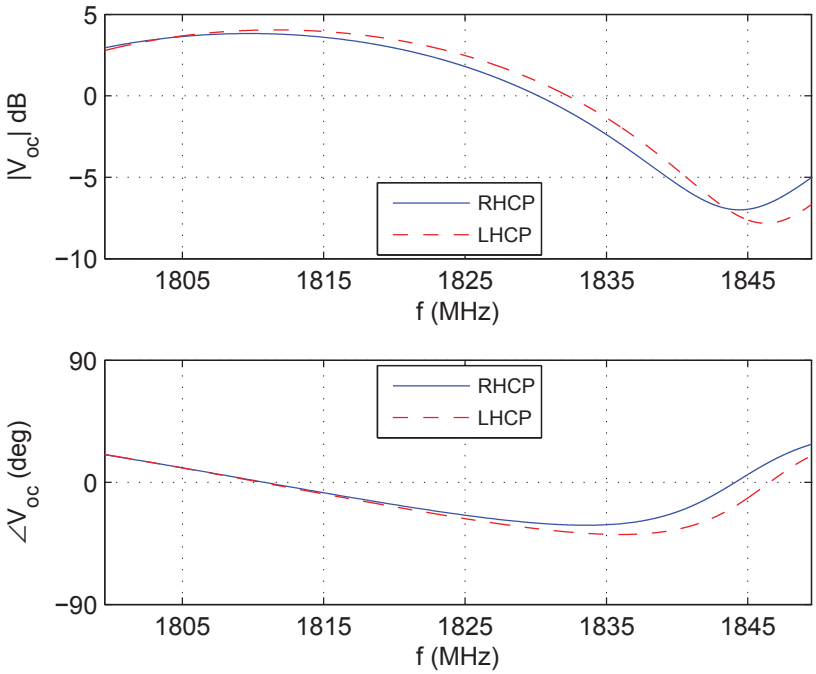

Figure 3.9: The simulated frequency response for the event shown in Figure 3.8.

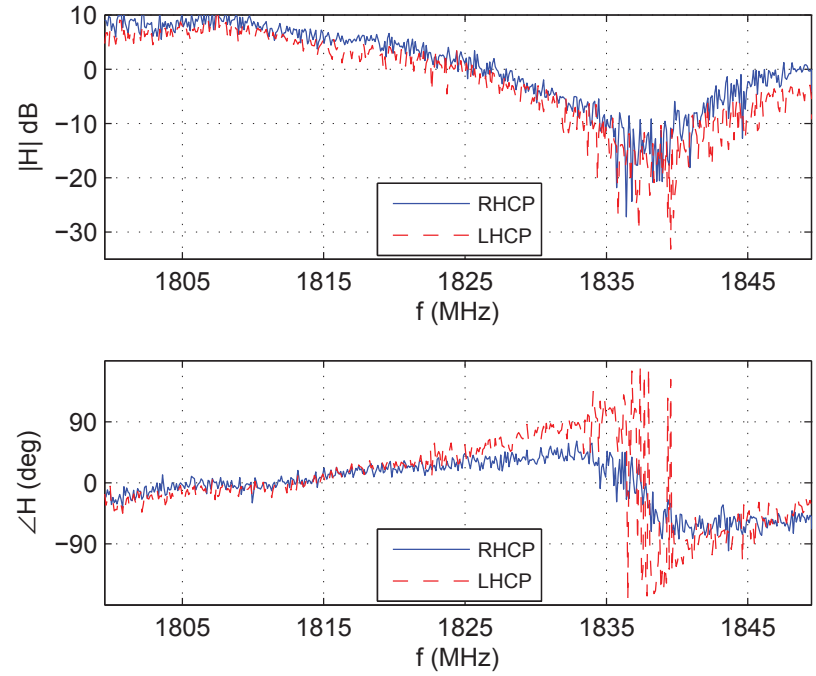

Figure 3.10: The frequency response from transmitter 1 from the channel sounding experiment during the event shown in Figure 3.8

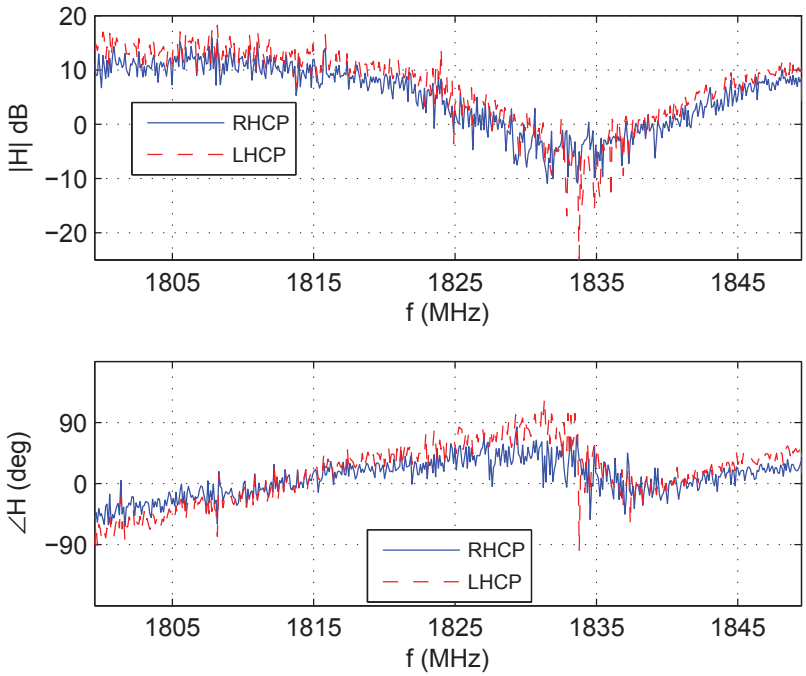

Figure 3.11: The frequency response from transmitter 2 from the channel sounding experiment during the event shown in Figure 3.8

3.3 Error Analysis

In the previous section we noted differences in the location of the nulls in the frequency responses of the simulated and real data. To determine if these differences can be accounted for due to small inaccuracies in the geometry of the events, we calculate how the location of the null changes with respect to small changes in the geometry.

The location of the nulls in the frequency response depends on the delay of the mulipath reflection wave due to the path length difference and the phase of the reflection coefficient. The impulse response is

$$h(t) = \delta(t) + \Gamma e^{-j\omega_c \tau}\delta(t-\tau) \tag{3.1}$$

where $\Gamma = |\Gamma|e^{j\gamma}$ is the reflection coefficient, ω_c is the carrier frequency in rad/s, and the delay is

$$\tau = \frac{2(h_t - h_s)(h_r - h_s)}{Rc} \tag{3.2}$$

where R is the range between the transmitter and reflector, h_t, h_s, and h_r are the heights of the transmitter, scattering surface, and receiver respectively as shown in Figure 3.12, and c is the propagation velocity. (Here we use $c = 3x10^8$ m/s, the propagation velocity in free space.) The frequency response is

$$H(f) = 1 + \Gamma e^{-j\omega_c \tau} e^{-j\omega\tau}, \tag{3.3}$$

and

$$|H(f)|^2 = 1 + |\Gamma|^2 + 2|\Gamma|\cos\left(\omega\tau + \omega_c\tau - \gamma\right). \tag{3.4}$$

Figure 3.13 shows the relationship between the nulls, delay, reflection coefficient and the bandwidth.

The null-to-null period is

$$\Delta f = \frac{1}{\tau} = \frac{cR}{2(h_t - h_s)(h_r - h_s)}. \tag{3.5}$$

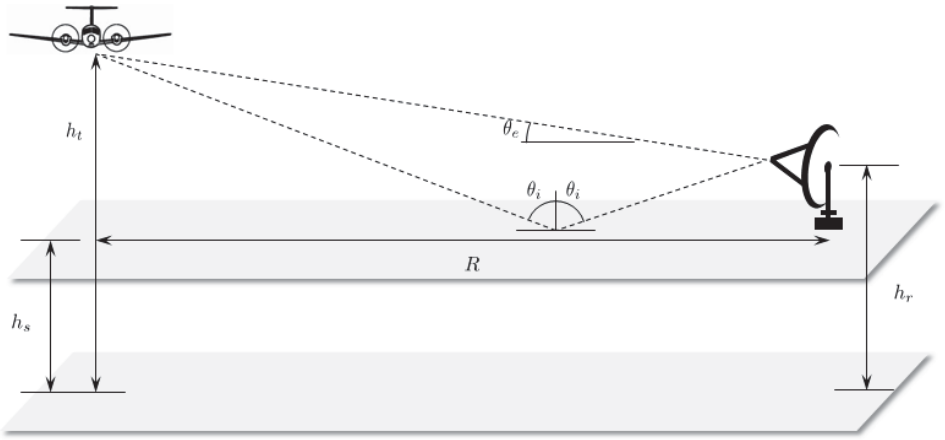

Figure 3.12: System model: Lower plane is AMSL and upper plane is the reflecting surface.

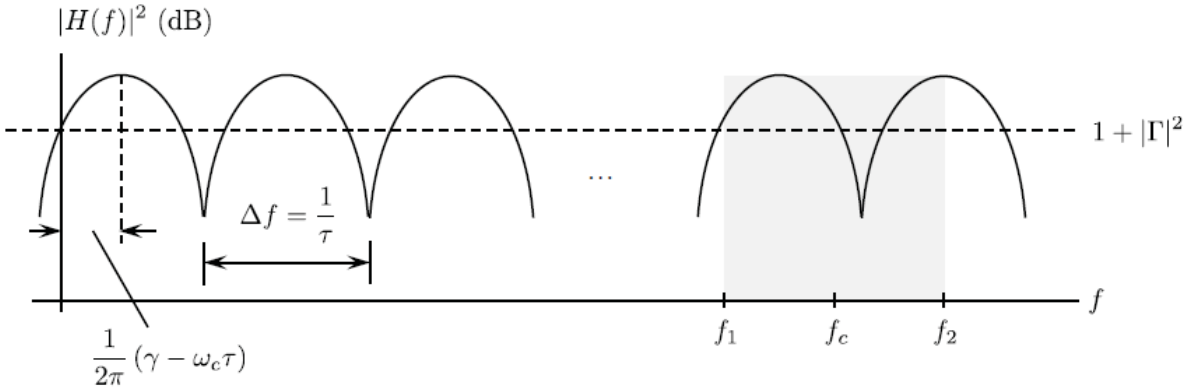

Figure 3.13: The relationship between the nulls, delay (τ), and the bandwidth. f_1 and f_2 are the smallest and largest frequencies in the bandwidth, respectively

The location of the null that falls within our bandwidth can be found as

$$f_n = Q\Delta f + \frac{\gamma - \omega_c \tau}{2\pi} \tag{3.6}$$

where f_1 is the lowest frequency in the bandwidth (see Figure 3.13), and Q is the integer given by

$$Q = \left\lceil \frac{f_1 - \frac{\gamma - \omega_c \tau}{2\pi}}{\Delta f} \right\rceil \tag{3.7}$$

Using the geometry in Event 1, $\Delta f = 70$ MHz. Because the bandwidth is only 50 MHz, there will not always be a null found within the bandwidth. So f_n will actually find the first null after f_1. To see how f_n changes with respect to small changes in the geometry, we take the derivative with respect to the variable that is changing (h_t or h_s or R).

$$\frac{\partial f_n}{\partial x} = \frac{\partial Q}{\partial x}\Delta f + Q\frac{\partial \Delta f}{\partial x} + \frac{1}{2\pi}\frac{\partial \gamma}{\partial x} - \frac{\omega_c}{2\pi}\frac{\partial \tau}{\partial x} \tag{3.8}$$

where x is h_t or h_s or R. For small changes in the geometry $\partial Q/\partial x$ and $\partial \gamma/\partial x$ are both 0. So (3.8) simplifies to

$$\frac{\partial f_n}{\partial x} = Q\frac{\partial \Delta f}{\partial x} - \frac{\omega_c}{2\pi}\frac{\partial \tau}{\partial x}. \tag{3.9}$$

Taking the derivative with respect to R, h_t and h_s and using the geometry of Event 1 gives

$$\frac{\partial f_n}{\partial R} = \frac{Qc}{2(h_t - h_s)(h_r - h_s)} + \frac{\omega_c}{2\pi}\frac{2(h_t - h_s)(h_r - h_s)}{cR^2} = 23.1 \text{ kHz/M}, \tag{3.10}$$

$$\frac{\partial f_n}{\partial h_t} = -\frac{QRc}{2(h_t - h_s)^2(h_r - h_s)} - \frac{\omega_c}{2\pi}\frac{2(h_r - h_s)}{cR} = \text{-2.25 MHz/M} \tag{3.11}$$

and

$$\frac{\partial f_n}{\partial h_s} = -\frac{QRc}{2}\frac{2h_s - h_t - h_r}{(h_t h_r - h_t h_s - h_r h_s + h_s^2)^2} - \frac{\omega_c}{2\pi}\frac{2(2h_s - h_t - h_r)}{cR} = 11.1 \text{ MHz/M}. \tag{3.12}$$

These results show that the differences seen between the simulated frequency response and the real data shown in Figures 3.5, 3.6 and 3.7 can very easily be accounted for as inaccuracies in the height of the reflecting surface or the height of the transmitters.

Also, the difference in the location of the nulls found in Figures 3.6 and 3.7 can be accounted for by the difference in the height of the transmitters. Transmitter 1 is mounted on the underside of the plane and transmitter 2 is mounted. Figure 3.1 shows the vertical displacement between them to be 1.765m.

Chapter 4

Conclusions

The question we set out to answer was this: Is there any potential for diversity gain with RHCP and LHCP signals in the presence of multipath propagation typically observed in aeronautical telemetry? To answer the question, in chapter 2 we derived the open-circuit voltage at the output of vertical and horizontal antenna elements and used these voltages to obtain expressions for the LHCP and RHCP voltages synthesized in an antenna feed. Multipath propagation was modeled by a specular ground (or ocean) bounce. Evaluation of the expressions for some realistic scenarios showed that it is often the case that the LHCP and RHCP voltage phasors are different.

In chapter 3 we compared the model derived in chapter 2 to experimental data obtained at EAFB. We found close agreement between the model and experimental data. There are scenarios where the LHCP and RHCP voltages are different and because of these differences there is potential for diversity improvement, but the precise method for exploiting that diversity remains to be worked out.

Bibliography

[1] C. Balanis, *Advanced Engineering Electromagnetics*. New York: John Wiley & Sons, 1989. 3, 5, 6, 7

[2] M. Rice, A. Davis, and C. Bettwieser, "A wideband channel model for aeronautical telemetry," *IEEE Transactions on Aerospace and Electronic Systems*, vol. 40, no. 1, pp. 57–69, January 2004. 4, 13

[3] Q. Lei and M. Rice, "Multipath channel model for over-water aeronautical telemetry," *IEEE Transactions on Aerospace and Electronic Systems*, vol. 45, no. 2, pp. 735 – 742, April 2009. 4

[4] K. Warnick and M. Jensen, class notes for ECEn 665: Antennas and Propagation for Wireless Communications, Brigham Young University, Winter Semester 2013. 8

[5] M. Rice, "Multipath modeling and mitigation using multiple antennas," Brigham Young University, Tech. Rep., 2013. 18

[6] ——, "A comparison of L-band and C-band multipath propagation at Edwards AFB," in *Proceeding of th Internation Telemetering Conference*, Lav Vegas, NV, 2011. 18